Clim Dyn (2016) 46:1877–1891
DOI 10.1007/s00382-015-2681-3

Abrupt intensification of ENSO forced by deglacial ice-sheet retreat in CCSM3

Zhengyao Lu[1] · Zhengyu Liu[1,2] · Jiang Zhu[2]

Received: 27 November 2014 / Accepted: 20 May 2015 / Published online: 10 June 2015

Abstract The influence of ice-sheet retreat on the El Niño–Southern Oscillation (ENSO) variability is studied using a transient simulation in NCAR-CCSM3 forced only by variations in continental ice sheets during the last deglaciation. The most striking feature is an abrupt strengthening of ENSO (by ~25 %) at 14 thousand years before present (ka BP) in response to a significant retreat (an equivalent ~25 m sea-level rise) of the Laurentide ice sheet (LIS). This abrupt intensification of ENSO is caused mainly by a sudden weakening of the equatorial annual cycle through the nonlinear mechanism of frequency entrainment, rather than an increase in the coupled ocean–atmosphere instability. The weakened annual cycle corresponds to a reduced north–south cross-equatorial annual mean SST contrast in the eastern Pacific. This reduced interhemispheric SST gradient—significant cooling north of the equator—is forced predominantly by an anomalous easterly from an abrupt polarward shift of the jet stream in the Northern Hemisphere, which extends to the northeastern tropical Pacific Ocean surface and is reinforced by the wind-evaporation-SST feedback then propagates equatorward; it could also be contributed by a fast sea-ice expansion and a consequent cooling in the North Pacific and North Atlantic that is induced by the retreat of the LIS.

Keywords ENSO · Annual cycle · Frequency entrainment · Deglacial ice-sheet forcing

1 Introduction

El Niño–Southern Oscillation (ENSO) is the most significant interannual climate variability in the climate system (Neelin et al. 1998; McPhaden et al. 2006), and has a significant global impact through atmospheric teleconnections (Trenberth et al. 1998; Liu and Alexander 2007). Past climate records depict substantial changes of ENSO intensity. In spite of intractable uncertainties, most past records suggest an intensification of ENSO in the Holocene (Tudhope et al. 2001; Moy et al. 2002; Rein et al. 2005; Conroy et al. 2008; Koutavas and Joanides 2012; Cobb et al. 2013; Carré et al. 2014). Most climate models also simulate an intensified ENSO from mid-to-late Holocene as a response to the precessional forcing (e.g., Liu et al. 2000; Clement et al. 2000; Otto-Bliesner et al. 2003; Timmermann et al. 2007a; Zheng et al. 2008; Masson-Delmotte et al. 2013). In comparison, proxy records for ENSO change during the early deglaciation are very limited and are often inconsistent among proxies (Liu et al. 2014). Modeling studies on the ENSO change at the Last Glacial Maximum (LGM) also show considerable spread among models (Otto-Bliesner et al. 2003; Zheng et al. 2008; Masson-Delmotte et al. 2013). The complexity of the ENSO response at the LGM can be attributed to the multiple forcings at the LGM, notably, the greenhouse gases and the ice sheet. The effect of the changing greenhouse gases on ENSO has been studied intensively, mostly in the context of future climate change

Electronic supplementary material The online version of this article (doi:10.1007/s00382-015-2681-3) contains supplementary material, which is available to authorized users.

✉ Zhengyao Lu
luzhengyao88@gmail.com; zlu@pku.edu.cn

[1] Laboratory for Climate, Ocean and Atmosphere Studies, School of Physics, Peking University, Beijing 100871, People's Republic of China

[2] Department of Atmospheric and Oceanic Sciences and Nelson Center for Climatic Research, University of Wisconsin-Madison, Madison, WI 53706, USA

(Guilyardi 2006; van Oldenborgh et al. 2005; Meehl et al. 2006, 2007; Collins et al. 2010), whereas the effect of ice sheet on ENSO, to our knowledge, has not yet been studied. The retreating ice sheets since the LGM (Dyke 2004) are associated with extraordinary change in both orography and surface albedo and therefore may potentially exert significant climate impact on the coupled ocean–atmosphere system in the tropics (e.g., Russell et al. 2014; Lee et al. 2014) and, in turn, on ENSO.

Our study of the effect of ice sheet on ENSO is also motivated by our efforts to understand the evolution of ENSO in the last 21,000 years in a transient simulation in the NCAR-CCSM3 that is forced by the transient forcings of the ice sheets, melt water flux, insolation and atmospheric greenhouse gases (TRACE) (Liu et al. 2014). Previous studies suggest that TRACE can capture the major characters of climate evolution during the last 21,000 years (Liu et al. 2009; Shakun et al. 2012), giving us some confidence in the model's capability in simulating deglacial climate changes. In terms of the ENSO variation in TRACE, our recent study (Liu et al. 2014) shows a gradual intensification of ENSO in the Holocene, which is qualitatively consistent with most proxy records and lies within the spread of PMIP2/PMIP3 ensemble experiments. On contrast, the simulated ENSO evolution exhibits a complex variation pattern before the Holocene during the early deglaciation, when the climate is forced by the varying melt water fluxes, insolation, greenhouse gasses and the continental ice sheets. The model-data and inter-model comparisons are challenging because of rare and less robust observations and worse agreement between models, while the latter could be induced by the competing effects of ice-sheet and atmospheric CO_2 forcings.

Thus, it is necessary to isolate the role of ice sheets, especially when those forcings often change simultaneously. Here we investigate ENSO response to the ice-sheet changes systematically in a transient simulation of the last 19,000 years forced only by variations in continental ice-sheets (hereafter ICE, He et al. 2013). It is found that ENSO is intensified abruptly at 14 ka BP, but otherwise is changed little. At 14 ka BP, the retreat of North American ice sheet shifts the atmospheric jet stream northward, which intensifies trade wind in the tropical northeastern Pacific, leading to a reduced cross-equatorial annual mean SST gradient in the eastern Pacific and in turn a weaker equatorial annual cycle. The reduced annual cycle eventually intensifies ENSO through the nonlinear mechanism of frequency entrainment. In addition, sea ice expands in the North Pacific and North Atlantic in response to the retreating ice sheet can potentially contributes to the reduced SST meridional gradient, weakened annual cycle and in turn ENSO intensification. The paper is arranged as follows. Section 2 briefly describes the model and experimental setting. Section 3 shows the response of the global climatology and ENSO to the receding ice sheets, and examines both linear and nonlinear mechanisms for ENSO change. Section 4 investigates the possible cause triggering the transition in tropical mean climate. A discussion and a summary are in Sects. 5 and 6, respectively.

2 Model and simulation

In order to test the global climatic impact of the ice-sheet retreat, the ICE simulation of the last 19,000 years was performed in NCAR-CCSM3 forced only by the deglacial evolution of the continental ice sheets (He et al. 2013). The model has a low resolution (Yeager et al. 2006; Otto-Bliesner et al. 2006). The atmospheric model is the Community Atmospheric Model 3 (CAM3), with a ~3.75° latitude–longitude resolution (T31) and 26 hybrid coordinate levels in the vertical. The land model also has a T31 resolution, and each grid box includes a hierarchy of land units (glaciers, lakes, wetlands, urban areas, and vegetated regions can be specified), soil columns, and plant types. The ocean model is the NCAR implementation of the Parallel Ocean Program (POP), with a ~3.6° longitudinal resolution, a variable latitudinal resolution (~0.9° near the equator, gx3v5) and 25 vertical z coordinate levels. The sea ice model is the NCAR Community Sea Ice Model (CSIM), a dynamic-thermodynamic model that includes a subgrid-scale ice thickness distribution. The resolution of CSIM is identical to that of POP.

In experiment ICE, the ice sheets were prescribed as the lower boundary condition to the atmosphere on the time resolution of the ICE-5G (VM2) reconstruction (Peltier 2004), varying from once every 1000 years (from 19 to 17 ka BP) to 500 years (after 17 ka BP). The model was integrated from the simulated glacial state at 19 ka BP (Liu et al. 2009) with all other forcings fixed as the same values as at 19 ka BP.

3 The response of ENSO and its mechanism

3.1 The response of ENSO to deglacial retreat of ice sheets

We first describe the evolution of some major climate features forced by the retreat of ice sheets in ICE. Figure 1a shows the evolution of the global ice-sheet volume. Starting from 19 ka BP, the volume of NH ice sheets (solid black line) first decrease gradually by an equivalent sea-level of 25 m from 19 to 14 ka BP, then dramatically by another 25 m associated with the Melting Water Pulse 1A event at 14 ka BP, and finally by ~50 m to the modern condition from

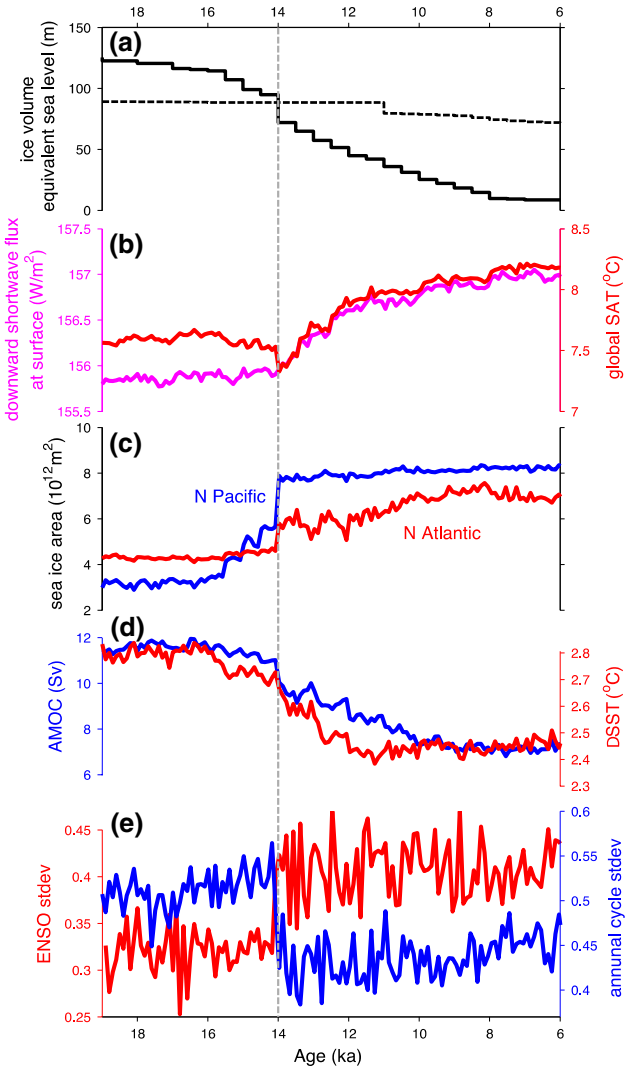

Fig. 1 19–6 ka BP time series of ICE experiment. **a** The North Hemisphere (*solid*), the South Hemisphere (*dashed*) ice volume converted from ICE-5G reconstruction (as equivalent sea-level rise) and used by model. **b** Simulated global net downward shortwave flux (*purple*) and global mean SAT (*red*). **c** Modeled sea-ice extent for North Atlantic sector (*blue*) and North Pacific sector (*red*) (regions are illustrated in Fig. 7i map). **d** Modeled AMOC (*blue*) and area-weighted mean SST difference of the North Hemisphere minus the South Hemisphere (*red*). **e** ENSO Amplitude (*red*) of Nino3.4 region calculated as standard deviation of monthly SST filtered through a 1.5–7 year band, and annual cycle amplitude (*blue*) both in 100-year windows. The modeled mean states in (**b**)–(**d**) are also in 100-year windows. The *vertical dashed line* depicts the 14 ka BP threshold

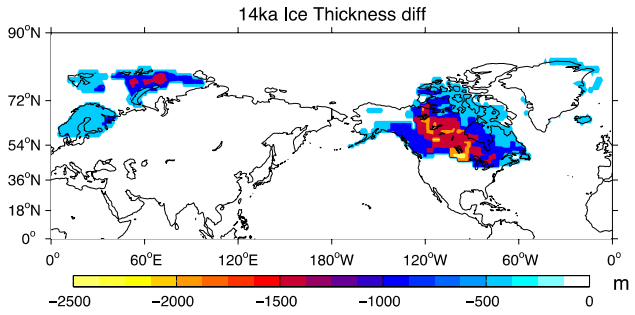

Fig. 2 Ice-sheet thickness difference of 13–15 ka BP in the NH

14 to 7 ka BP. Most of the changes come from the lowering of the Laurentide and Fennoscandian ice sheets. Particularly at 14 ka BP there is over 500 m of elevation decrease of LIS across Canada, northern US and Alaska, which accounts for ~88 % of the drop in NH ice-sheet volume, with the largest reduction in the western Canada by over 1000 m (Fig. 2). Nevertheless in the Southern Hemisphere (SH) the loss of ice-sheet volume is one order smaller (dashed black line), only of ~20 m sea-level rise, with the major change (~8 m) occurring at 11 ka BP. The continuing retreating of the continental ice sheet reduces the planetary albedo and therefore gradually increases the global mean net downward shortwave flux at surface (Fig. 1b, purple line). The simulated global mean surface air temperature (SAT) (Fig. 1b, red line) is then increased by 0.7 °C since the 19 ka BP. However, instead of following the gradual reduction of the ice-sheet volume and albedo, the global temperature exhibits a clear warming only after 14 ka BP, suggesting a nonlinear response of global SAT to ice-sheet retreat associated with both the albedo feedback and orographic effect. In the meantime, the sea-ice extent in the North Atlantic and North Pacific (Fig. 1c) expands significantly, with the major increase occurring at 14 ka BP. The increased albedo associated with the sea-ice expansion can partly compensate for the reduced albedo associated with the loss of continental ice (especially at 14 ka BP, Supplementary material 2, Fig. S2), mitigating the outgoing radiation followed by global warming. The retreating ice sheets also causes a slow weakening of the Atlantic Meridional Overturning Circulation (AMOC) from 11.5 to 7 Sv (Fig. 1d, blue line), because of the northward shift of the NH westerly and the resulting eastward sea-ice expansion and enhanced insulating effect over the North Atlantic (Zhu et al. 2014). The suppressed AMOC can further induce a bipolar seesaw response by reducing the oceanic heat transport into the NH and can lead to a smaller N–S interhemispheric SST gradient (Fig. 1d, red line) (Crowley 1992; Stocker and Johnsen 2003).

In spite of the gradual retreat of ice sheets, ENSO intensity (Fig. 1e, red line), which is calculated as the standard deviation of the Nino3.4 SST within the frequency band of 1.5–7 year, shows a sudden increase at 14 ka BP but otherwise remains largely unchanged, albeit with a strong inherent irregularity (Cobb et al. 2013). At 14 ka BP, ENSO is intensified abruptly by ~25 %, accompanied by a concurrent abrupt weakening of the equatorial annual cycle (Fig. 1e, blue line). Furthermore, the Hovmoller diagrams (Fig. 3) depict that the ENSO variability dominates the central/eastern Pacific while annual cycle prevails in the

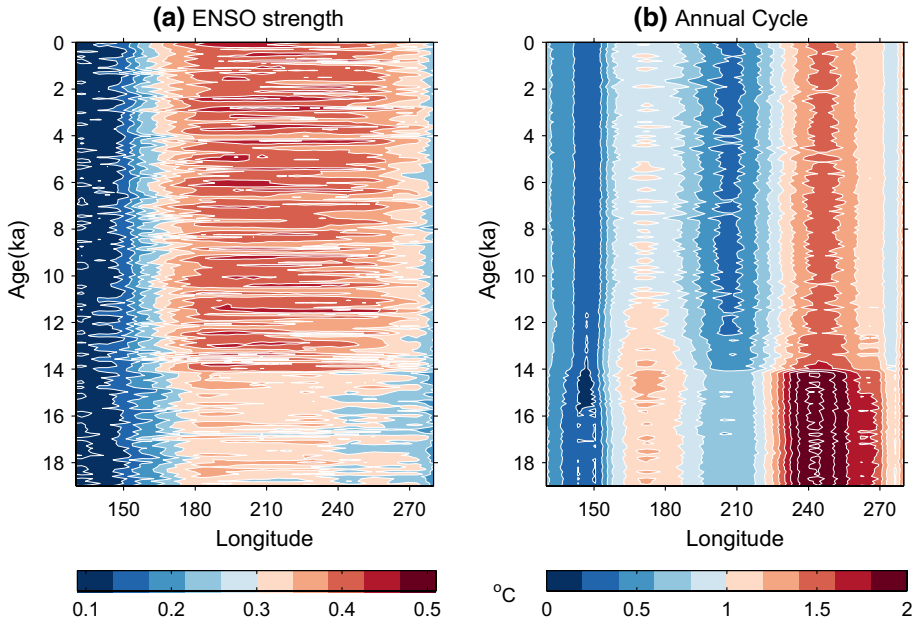

Fig. 3 Evolution of ICE SST variability in the equatorial Pacific (5°N–5°S, 130°E–80°W). **a** Standard deviation of interannual SST variability (1.5–7 year); **b** standard deviation of the annual cycle, both using 100-year windows

eastern Pacific (Philander et al. 1996). Evidently, the 14 ka BP shifts occur across the central Pacific for ENSO and the eastern Pacific for annual cycle. The former implies a potential threshold behavior of the response of tropical climate variability to ice-sheet retreat; the opposite change of the latter indicates that the ENSO strength could be influenced by its nonlinear interaction with the annual cycle, a point to be returned later. On contrast, the ENSO frequency stays unchanged (~biennial) throughout the simulation (Supplementary material 1, Fig. S1). The major questions are therefore: How does the ice-sheet retreat intensify ENSO amplitude? Why is ENSO intensified abruptly at 14 ka BP, but is changed little from 19 to 14 ka BP or from 14 to 6 ka BP, when the NH ice sheet also decreases with a comparable amount as at 14 ka BP? These questions will be addressed in the following sections.

3.2 Mechanisms for changes in ENSO variability

3.2.1 Linear stability in terms of the BJ index

We first examine the role of ocean–atmosphere feedback in terms of the Bjerknes stability (BJ) index, which is a measure of the linear coupled ocean–atmosphere instability (Jin et al. 2006). To quantify the effects of different feedbacks, we calculate each term of the BJ index. The linearized SST tendency equation in the mixed layer is:

$$\frac{\partial T}{\partial t} = Q - \frac{\partial(\bar{u}T)}{\partial x} - \frac{\partial(\bar{v}T)}{\partial y} - \frac{\partial(\bar{w}T)}{\partial z} - u\frac{\partial \bar{T}}{\partial x} - v\frac{\partial \bar{T}}{\partial y} - w\frac{\partial \bar{T}}{\partial z} \quad (1)$$

We average Eq. (1) spatially over a rectangular box of the tropical central and eastern Pacific Ocean (5°S–5°N, 180°E–80°W) following Kim and Jin (2011a, b). Denoting the averaged variables in $\langle\rangle$, it becomes:

$$\frac{\partial\langle T\rangle}{\partial t} = \langle Q\rangle - \left(\frac{(\bar{u}T)_{EB} - (\bar{u}T)_{WB}}{Lx} + \frac{(\bar{v}T)_{NB} - (\bar{v}T)_{SB}}{Ly}\right) - \left\langle\frac{\partial \bar{T}}{\partial x}\right\rangle\langle u\rangle - \left\langle\frac{\partial \bar{T}}{\partial z}\right\rangle\langle H(\bar{w})w\rangle + \left\langle\frac{\bar{w}}{H_1}\right\rangle\langle H(\bar{w})T_{sub}\rangle \quad (2)$$

where

$$H(x) = \begin{cases} 1, & x \geq 0 \\ 0, & x < 0 \end{cases}$$

is the step function. Assuming we have:

$$\frac{\partial\langle T\rangle}{\partial t} \approx R\langle T\rangle$$

then the BJ index (R) can be derived as:

$$R = \underset{\text{TD}}{-\alpha_s} \underset{\text{MA}}{-\alpha_{MA}} + \underset{\text{ZA}}{\mu_a\beta_u\langle -\bar{T}_x\rangle} + \underset{\text{EK}}{\mu_a\beta_w\langle -\bar{T}_z\rangle} + \underset{\text{TH}}{\mu_a\beta_h\left\langle\frac{\bar{w}}{H_1}\right\rangle a_h} \quad (3)$$

while in Eq. (3) the coefficients $\alpha_s, \alpha_{MA}, \mu_a, \beta_u, \beta_w, \beta_h, a_h$ can be calculated using least-square regression method (Kim and Jin 2011a, b; see also Liu et al. 2014 Methods for more details). The BJ index is a sum of five feedback terms, including two negative feedbacks (the surface heat flux feedback, or thermodynamic damping, TD; the mean advection feedback, or dynamic damping, MA) and three positive feedbacks (the zonal advection feedback, ZA; the Ekman local upwelling feedback, EK; the thermocline

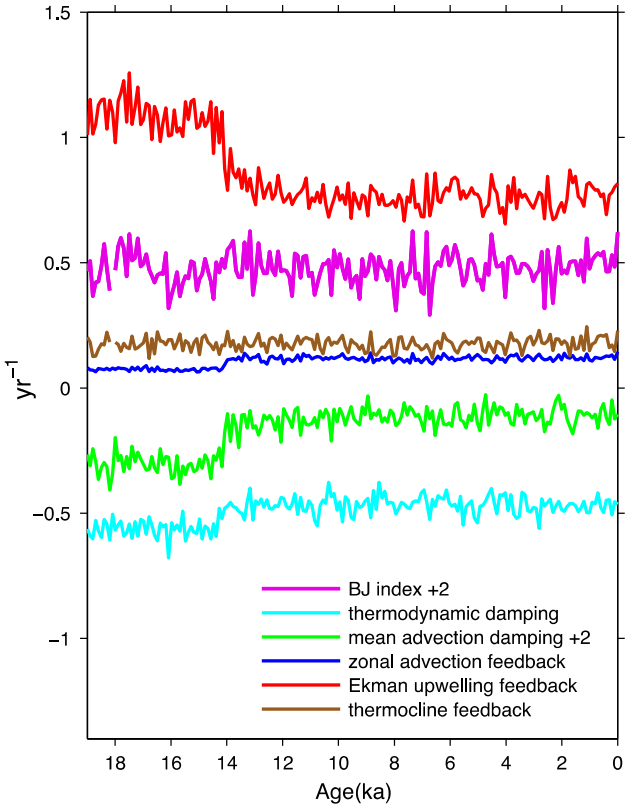

Fig. 4 Time series of contributing terms in the BJ index formula: thermodynamic damping (TD, *cyan*), the mean advection damping (MA, *green*), the zonal advection feedback (ZA, *blue*), the thermocline feedback (TH, *brown*), the Ekman upwelling feedback (EK, *red*), and BJ index (BJ, *purple*). Note that BJ and MA have both added an offset by 2

feedback, TH). The three dynamical positive feedbacks consist of the characteristics of the background states and the surface wind stress sensitivity responding to ENSO SST anomalies, as well as its own oceanic dynamic sensitivity responding to equatorial surface winds.

All these damping effects and feedbacks involved in the ENSO stability are compared in Fig. 4. It is found that TH and ZA do not change much throughout the simulation; EK decreases abruptly at 14 ka BP, but is compensated by the weakened damping in TD and MA. As a result the sum, the BJ index, remains almost unchanged. Given the abrupt intensification of ENSO strength at 14 ka BP and the relatively constant BJ index (Figs. 1e red line vs. 4 purple line), we conclude that the ENSO intensification at 14 ka BP cannot be explained by an increase in the coupled instability.

Figure 5 further shows the evolutions of the regression coefficients and mean states of different variables related to the three positive feedbacks: the upwelling feedback, the thermocline feedback and the zonal advection feedback. Despite the abrupt change of ENSO strength at 14 ka BP, most regression coefficients remain unchanged except for the atmospheric response μ_a and thermocline slope response β_h (Fig. 5a–d). The weakened atmospheric response is probably due to the tropical cooling (Fig. 8a), which is caused by the atmospheric teleconnection to the lowering of ice sheets. The thermocline slope response increases at 14 ka BP, but the change in the product of the coefficients is somehow canceled by the decreased atmospheric response. The mean states are also shifted at 14 ka BP, notably the increase of the zonal gradient of SST (Fig. 5e) and the decrease of stratification (Fig. 5f) in tropical Eastern Pacific. They indicate, to some extent, that the tropical Pacific climate might have exhibited an efficient, and possibly nonlinear, transition. Stationary regression coefficients and shifted mean states imply that the BJ terms (as their products, e.g., EK and ZA) would approximately follow the mean state change.

3.2.2 *ENSO–annual cycle nonlinear interaction*

The inconsistent evolutions of ENSO amplitude and BJ index suggest that the intensification of ENSO is not caused by an increased coupled instability. This leaves the frequency entrainment as an alternative mechanism for the ENSO response. The negative correlation between the amplitude of ENSO and annual cycle has been noticed in previous studies (e.g., Gu and Philander 1995; Guilyardi 2006) and can be explained in terms of the nonlinear mechanism of frequency entrainment (Liu 2002). The ENSO tends to give up its intrinsic oscillation mode by acquiring the frequency of an external periodic forcing that is close to its own eigenfrequency (i.e., the annual cycle). It might not work when the annual cycle is weak. However when a certain threshold is passed, ENSO's frequency is completely entrained into the forcing frequency of annual cycle and results in a substantial drop of interannual variability. This phenomenon is verified by conceptual model (Liu 2002), models with intermediate complexity (Chang et al. 1994, 1995) and coupled GCMs (Timmermann et al. 2007a, b). Liu et al. (2014) also propose that during the early deglaciation the large millennial fluctuations of ENSO amplitude is a result of interaction with equatorial annual cycle in response to meltwater discharges and the subsequent AMOC induced SST bi-polar seesaw.

Here, the amplified annual cycle seems to suppress ENSO variability in the equatorial Pacific, and vice versa, on the millennial time scales (Fig. 1e), as conveyed in the first sight of our experiment. There is a highly significant negative correlation between them (−0.69, for 19–0 ka BP). Moreover, it is evident that at 14 ka BP the abrupt increase of ENSO amplitude is accompanied by a sudden weakening of the annual cycle (Figs. 1e, 3a, b). Even on the centennial time scales, the irregular fluctuations in the

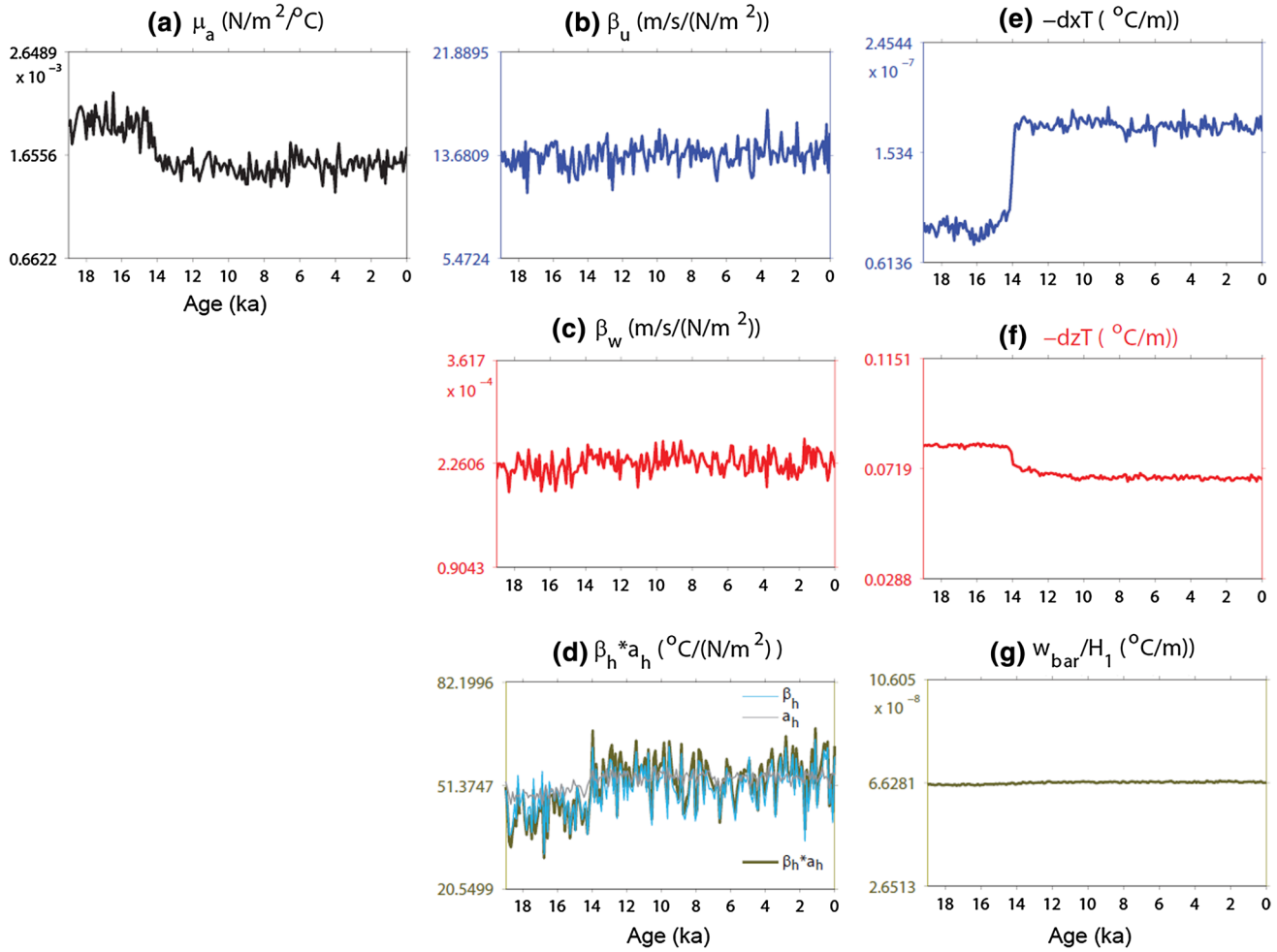

Fig. 5 Components of BJ terms. Regression coefficients for **a** μ_a, **b** β_u, **c** β_w, and **d** β_h * a_h, mean states for **e** −dxT, **f** −dzT and **g** $\overline{w}/H_1$

amplitude of ENSO and annual cycle tend to vary opposite to each other.

The close interaction between the annual cycle and ENSO is also consistent with the strong phase-locking of the ENSO during the whole simulation, that is, the peak of interannual SST anomaly tend to occur in boreal winter (Fig. 6). Without the robust nonlinear interaction with the annual cycle, the ENSO would not necessarily tend to peak in a preferred season (Neelin et al. 2000; Liu et al. 2014).

4 The response of mean climate state

We have identified the sudden decrease of annual cycle as the cause of the abrupt intensification of ENSO at 14 ka BP. The next question is why the annual cycle is decreased abruptly.

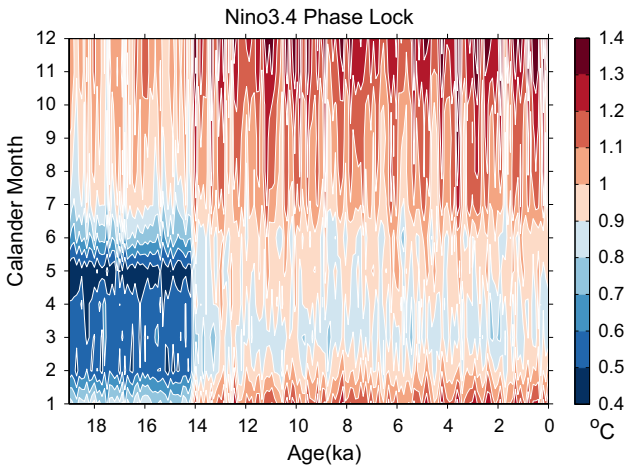

Fig. 6 Nino3.4 phase locking evolution (SST interannual variability as a function of time and calendar month)

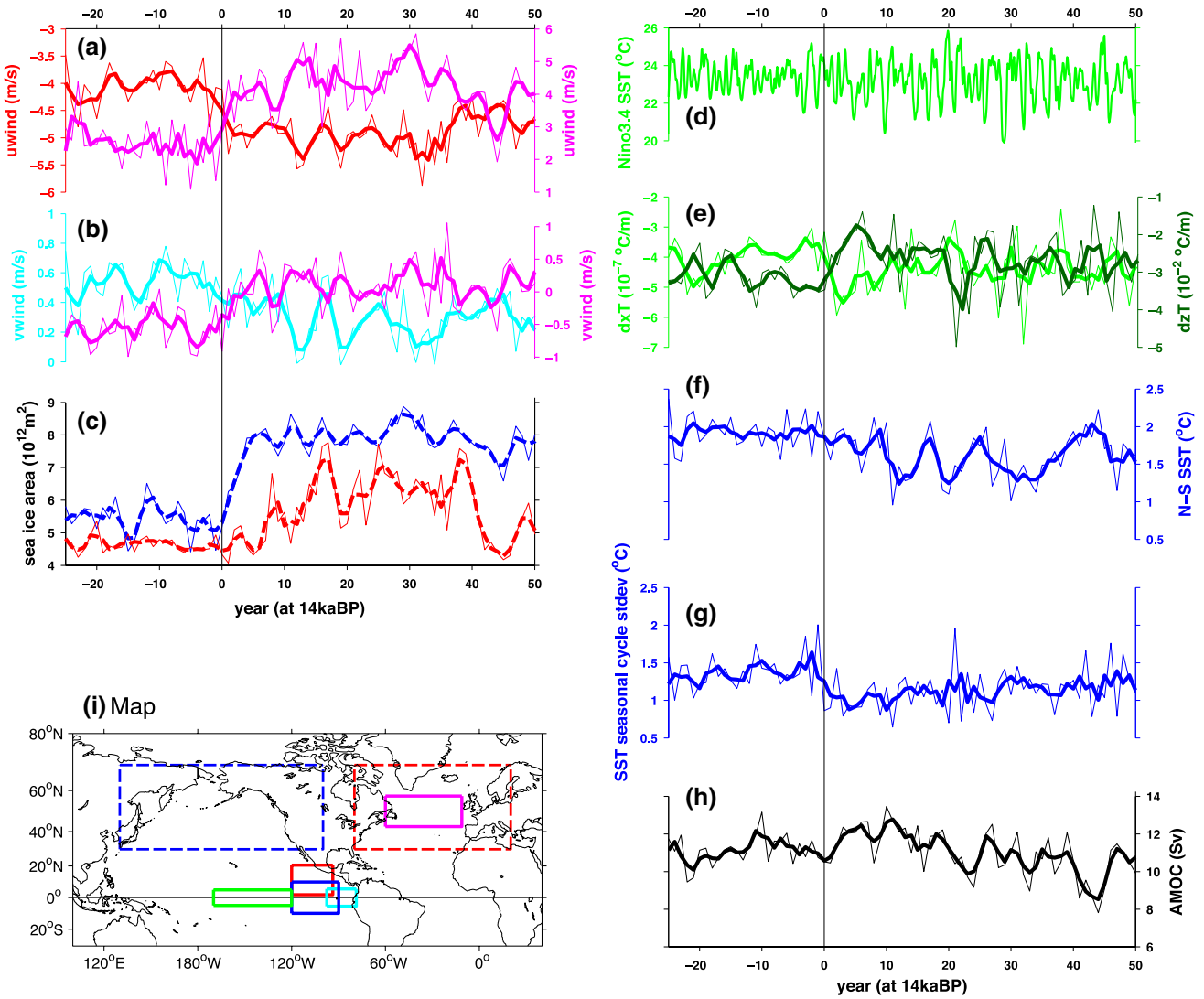

Fig. 7 Annual time series (**a**–**c** and **e**–**h**, *thick lines* are 3-year running mean) for **a** zonal low-level wind over tropical northeastern Pacific; downwind ice-sheet region; **b** meridional low-level wind over tropical eastern Pacific (cross-equator) and downwind ice-sheet region; **c** sea-ice extent in North Atlantic and North Pacific sectors; **d** monthly Nino3.4 SST (after 3-month running mean); **e** Nino3.4 SST dxT and dzT; **f** N–S SST gradient in the tropical eastern Pacific; **g** SST annual cycle in the tropical eastern Pacific; **h** AMOC. All time series are within time span of −25 before to +50 years after 14 ka BP. **i** *Boxes* in the map show the regions of the corresponding curves with the same *color* and line style

4.1 Response time scales

To understand the responses of the tropical climate to the lowering of ice sheets at 14 ka BP, we first examine the related response time scales. Figure 7 shows the annual time series of several key climate variables from −25 years before to +50 years after 14 ka BP. In spite of the significant inherent interannual variability, the 14 ka BP abrupt change is so large that its signal can be detected in the full time series. The surface wind field responds in <2 years after the lowering of the ice sheet, as seen in the intensification of the westerly (Fig. 7a, purple), the reversal of the northerly to southerly downwind of the LIS (Fig. 7b, purple) and the intensification of easterly in the tropical northeastern Pacific (Fig. 7a, red). The northerly cross-equatorial wind in the tropical eastern Pacific is weakened in ~5 years (Fig. 7b, cyan). The rapid response in the surface wind field suggests that the tropical Pacific climate is changed by the ice sheet mainly through the atmospheric teleconnection. At higher latitudes, sea ice expands in both North Atlantic and North Pacific sectors in <5 and 10 years, respectively (Fig. 7c).

The surface ocean also responds quickly in the central/eastern equatorial Pacific, for example the Nino 3.4 SST, the vertical temperature gradient, and the south to north cross-equatorial SST contrast (Fig. 7d–f, all in <10 years),

suggesting an efficient ocean–atmosphere coupling there. As a result, the amplitude of the SST annual cycle is decreased in <5 years (Fig. 7g). The increase of interannual SST variability is evident as seen in the Nino 3.4 SST time series (Fig. 7d). The SST interannual fluctuation amplifies in <10 years after 14 ka BP, accompanied by greater SST N–S gradient and reduced stratification (Fig. 7e) there. In contrast, the AMOC decreases gradually from ~11 to ~9 Sv in about 50 years (Fig. 7h). Therefore, the change of the climate mean state in the tropical eastern Pacific is most likely to be initiated by the rapid shift of the local wind and then enhanced by ocean–atmosphere coupling, rather than by the slow AMOC. However, it remains possible that the AMOC may influence the tropical eastern Pacific through the bipolar seesaw on multi-decadal time scale (Fig. 1d)—a point to be returned later.

4.2 Fast mean state changes suppress the annual cycle

Since the initial transition of the tropical Pacific mean climate is developed very abruptly (in a few years) at 14 ka BP, we will now focus on the spatial pattern of the response and the mechanism responsible for the suppressed annual cycle. The pattern of the rapid response can be seen in the difference of 50-year average of tropical Pacific climatology before and after 14 ka BP. Despite the seemingly zonally uniform response of the tropical Pacific in the Hovmoller diagrams (Fig. 3), the distributions of anomalies of the climate mean state are complicated. Among them the most remarkable feature in the eastern equatorial Pacific where the pronounced annual cycle exists (Fig. 3b) is the robust SST cooling (>1 °C) associated with increased trade wind (>0.01 N m^{-2}; >1 m s^{-1}) north of the equator (east of 120°W, Fig. 8a), as well as a weak SST warming with decreased trade wind to the west. The cooling with increased trade and warming with decreased trade indicate a potential contribution of the positive wind-evaporation-SST (WES) feedback through the ocean–atmosphere coupling (Xie and Philander 1994). The low-level wind anomaly is almost identical to wind stress anomaly (Fig. 8a, b), suggesting a corresponding low level wind field response, although the anomaly pattern split in the central Pacific and eastern Pacific. The SST anomaly is caused predominantly by the latent heat flux anomaly in the eastern equatorial Pacific (Fig. 8c, contour), except for the deep tropics, consistent with the role of WES feedback. In the deep tropics, increased trade induces a stronger equatorial upwelling in the eastern Pacific (Fig. 8b), contributing to the SST cooling there. Off the equator, surface heat flux at the ocean–atmosphere interface becomes important where the prevailing Ekman downwelling decouples SST from oceanic variability beneath. It is also interesting to observe a significant decrease in convective precipitation in the northeastern equatorial Pacific (Fig. 8c, shading), corresponding

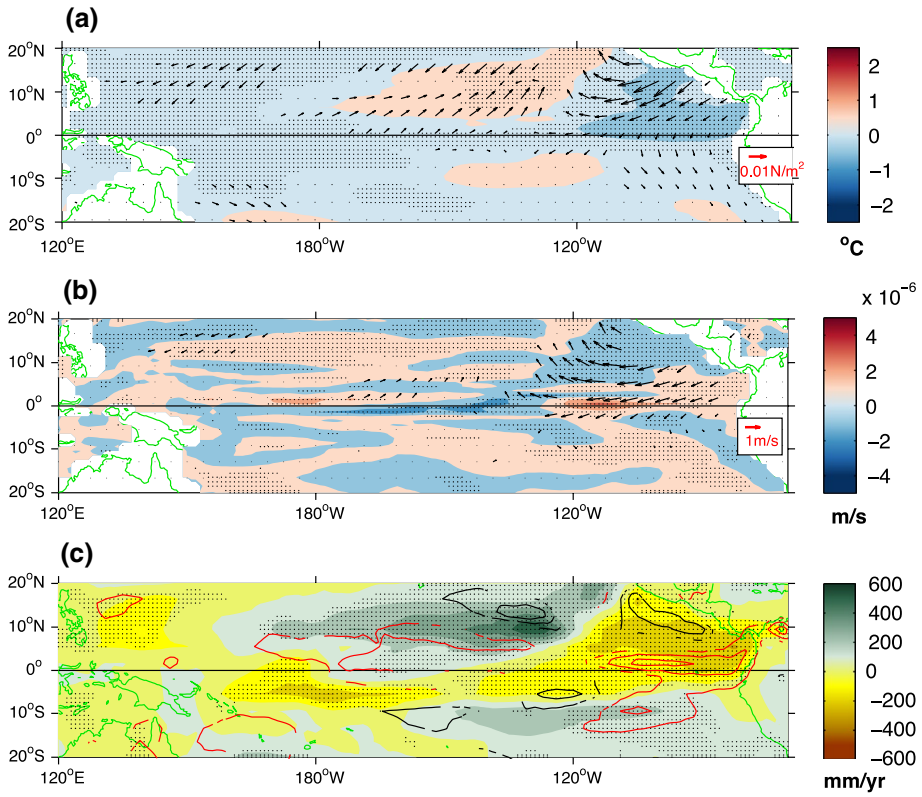

Fig. 8 Mean state difference distribution of 14 ka BP event, using 50-year mean after and before 14 ka BP, for tropical Pacific region. All differences displayed (or with stippling on) pass 95 % significance level. **a** SST and wind stress; **b** upwelling and 850–1000 hPa wind; **c** convective precipitation as *color* and latent heat flux as contour (*black* (*red*) for negative (positive), *contour* every 2 W m^{-2})

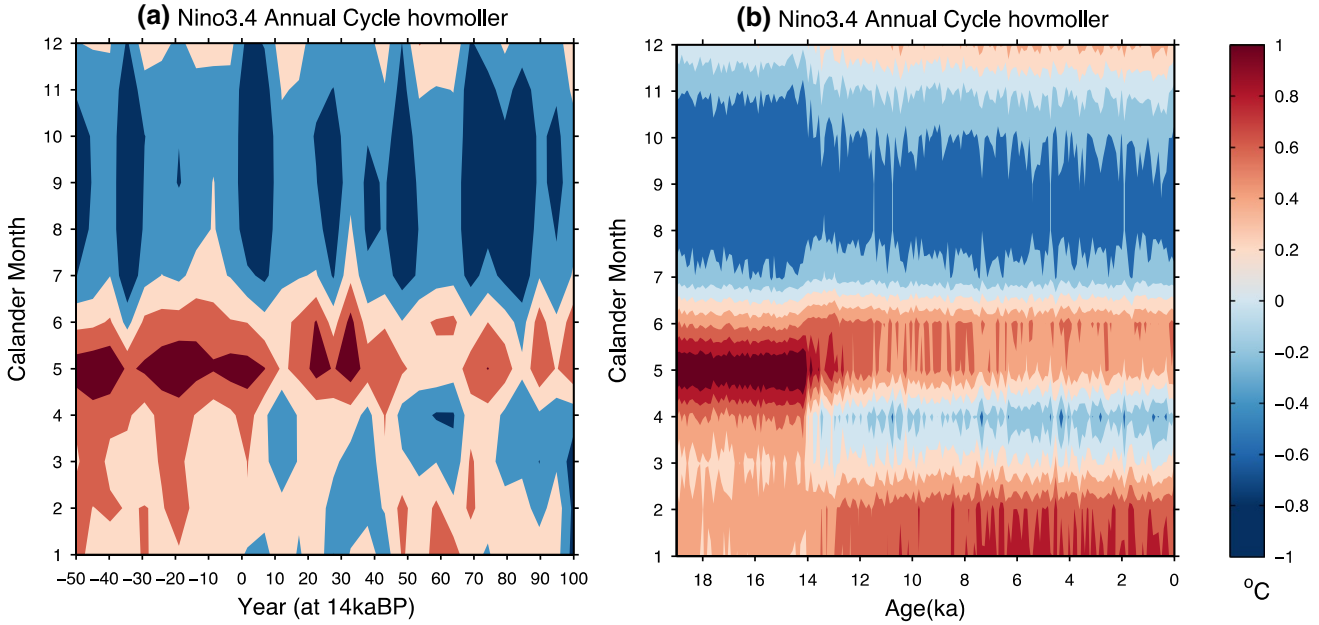

Fig. 9 Nino3.4 SST seasonal cycle evolution, derived from monthly SST subtracting climatology for **a** every 1 year during −60 before to +100 years after 14 ka BP and **b** every 100 years throughout 19,000 years

to the SST cooling. These characteristic features of the coupled SST/wind/surface heat flux/precipitation anomaly variations are in accordance with the significant role of WES feedback in maintaining such a SST N–S asymmetry in the tropical eastern Pacific.

The climatological ITCZ is located to the north of the equator, accompanied by a N–S asymmetry of SST in the central to eastern tropical Pacific with a warmer SST in the north, and a consequent annual cycle of SST in the eastern equatorial Pacific. The anomalous cooling asymmetry responding to the ice-sheet retreat at 14 ka BP (Fig. 8a) therefore reduces the N–S cross-equatorial SST gradient and suppresses the equatorial annual cycle, as shown in the Hovmoller diagram of annual cycle of SST near 14 ka BP in Fig. 9a. Immediately after 14 ka BP, the annual maximum temperature in early May of the Nino 3.4 SST is dampened significantly, associated with the uniform climatic shift of annual cycle amplitude across the tropical eastern Pacific (Fig. 3b). Moreover, the reduced SST annual cycle after 14 ka BP is accompanied by a weak semi-annual cycle, with two peaks in late May and late January (Fig. 9b). Overall, the annual cycle in the eastern equatorial Pacific is suppressed at 14 ka BP by a reduced N–S SST contrast.

4.3 The shift of jet stream as a trigger for the fast response of the tropical mean state climate

We have demonstrated the initial easterly anomaly over the tropical northeastern Pacific as the trigger for the WES feedback and, in turn, changes in the mean climate state of tropical Pacific. The next question is how the easterly anomaly is generated by the retreating ice sheets. Further analysis suggests that it is mainly contributed by the northward shift of NH jet stream.

The shift of jet stream in the NH is revealed by the Hovmoller diagram of 200 hPa zonal mean zonal wind (100–30°W) (Fig. 10a). Compared with its location at 19 ka BP, the jet center over the North America and North Atlantic, depicted by the location of maximum 200 hPa zonal wind, shifts northward abruptly at 14 ka BP from ~38 to 40°N and changes little throughout the Holocene. The strength of the jet decreases (Li and Battisti 2008), as the maximum zonal wind changes from >40 to ~35 m s^{-1} after the shift.

The annual mean jet streams travel at speeds >40 m s^{-1} at ~40°N in both hemispheres (Fig. 10b, c, contours). The spatial pattern of the fast response of the 200 hPa zonal wind at 14 ka BP suggests anomalous westerly centered at ~55°N and anomalous easterly centered at ~30°N over the North Pacific, North Atlantic and North American continent (Fig. 10b, shading). The wind anomaly is induced mainly by the shift rather than the change of tilt of jet stream over North America (Fig. 10b, c, black and purple contours). The northward shift of the jet stream is limited to the NH, because it is mainly forced by the retreating LIS. Previous studies also indicate the important role of ice-sheet topography on the large-scale atmospheric circulation (COHMAP 1988; Bartlein et al. 1998; Roe and Lindzen 2001; Eisenman et al. 2009; Pausata et al. 2011; Eagle et al. 2013; Zhang et al. 2014). The threshold response at

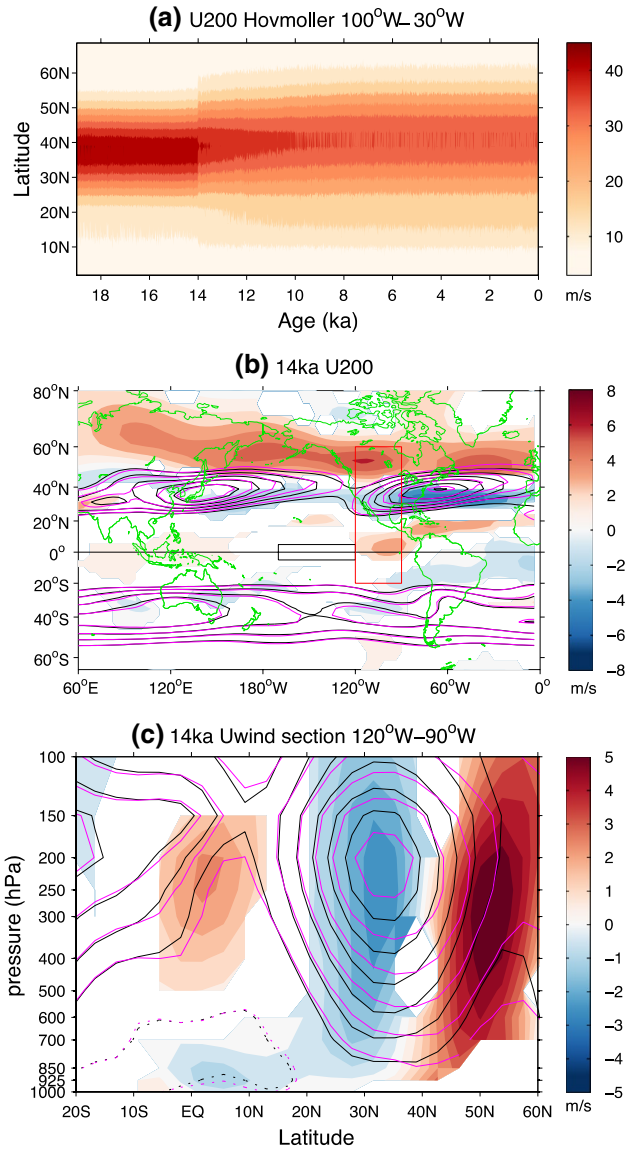

Fig. 10 **a** Hovmoller diagram of 200 hPa zonal wind averaged over North America and North Atlantic throughout 19,000 years; **b** 14 ka BP 200 hPa zonal wind mean state (*contour* every 5 m s^{-1} starting from 25 m s^{-1}) using 50-year average (*black/purple* is for before/after the ice-sheet retreat) and its anomaly (*shading*); *black box* is for Nino 3.4 region, *red box* depicts the spatial range in (**c**); **c** cross section of zonal mean zonal wind at 14 ka BP [*contour* every 5 m s^{-1}, *black solid* (*dashed*) *line* for westerly (easterly)] using 50-year average (*black/purple* is for before/after the ice-sheet retreat) and its anomaly (*shading*). All anomalies pass 95 % significance level

an intermediate height of ice sheet is similar to Lee et al. (2014) and Zhang et al. (2014).

The vertical cross-section of zonal mean zonal wind further confirms our argument that the abrupt polarward displacement of the jet stream can fundamentally impacts the wind fields in the tropics. The core of zonal wind over the lowering LIS abruptly shifts northward from ~35°N on the pressure level of 200 hPa (Fig. 10c, contours) after 14 ka BP. The shift leads to anomalous easterly (~5 m s^{-1}) in the previous jet stream center, which extends downward and southward to the lower troposphere (Fig. 10c, shading). The strengthened trade wind over the tropical eastern Pacific is therefore likely to be triggered by the shift of the jet stream. It is then reinforced and propagates equatorward through WES feedback (Xie and Philander 1994; Xie 1999). Over the equatorial northeastern Pacific (0–15°N) the near surface easterly anomalies have the magnitude of ~1 m s^{-1}, very significant given that the climatological zonal wind over there is ~5 m s^{-1}. The surface wind anomaly cools the SST north of the equator, reduces its N–S asymmetry, and in turn decreases the amplitude of the equatorial SST annual cycle in the eastern Pacific (Fig. 12). In the tropics, the easterly anomaly in the lower atmosphere (below 600 hPa) is also accompanied by a westerly anomaly aloft (Fig. 10c, shading), reflecting a baroclinic response of the tropical atmosphere to the jet shift in the mid-latitude through the atmospheric teleconnection.

4.4 Fast sea-ice expansion in the North Pacific and North Atlantic

In addition to the dynamic influence of the northward displacement of the jet stream, the expansion of sea ice in the North Pacific and North Atlantic may also contribute to the reduced N–S SST symmetry at 14 ka BP. The sea-ice expansion competes against the ice-sheet loss in the surface heat budget by altering radiative forcing, and has a fundamental impact on the global climate (Budikova 2009). As a consequence of receding LIS (Fig. 11b, cyan contours), consistent with earlier studies in idealized atmospheric models (Roe and Lindzen 2001; Jackson 2000) and AGCM (COHMAP 1988; Clark et al. 1999), the stationary wave pattern (anticyclone like) forced over vast ice-sheet topography is weakened and the westerly flows in a straighter path (Pritchard et al. 2008). This leads to a southward wind anomaly upstream the western slope of the LIS and over the eastern North Pacific, a northward wind anomaly over most of the lowering ice sheets and downstream over the North Atlantic basin (e.g., Eisenman et al. 2009; Lee et al. 2014), as well as the northward shifted westerly over the northern North Atlantic (Fig. 11a). The former can also strengthen the anti-cyclonic wind stress anomaly in the North Pacific which results in the weakening of Aleutian Low (Bartlein et al. 1998; Otto-Bliesner et al. 2006). These changes in wind stress are likely responsible for the more extensive sea-ice in both North Pacific and North Atlantic sectors a few years after the wind shift (Figs. 7a–c). The sea-ice expansions are caused by the increased export from regions of sea-ice formation, rather than by the increased local formation (Zhu et al. 2014). The sea-ice area expands

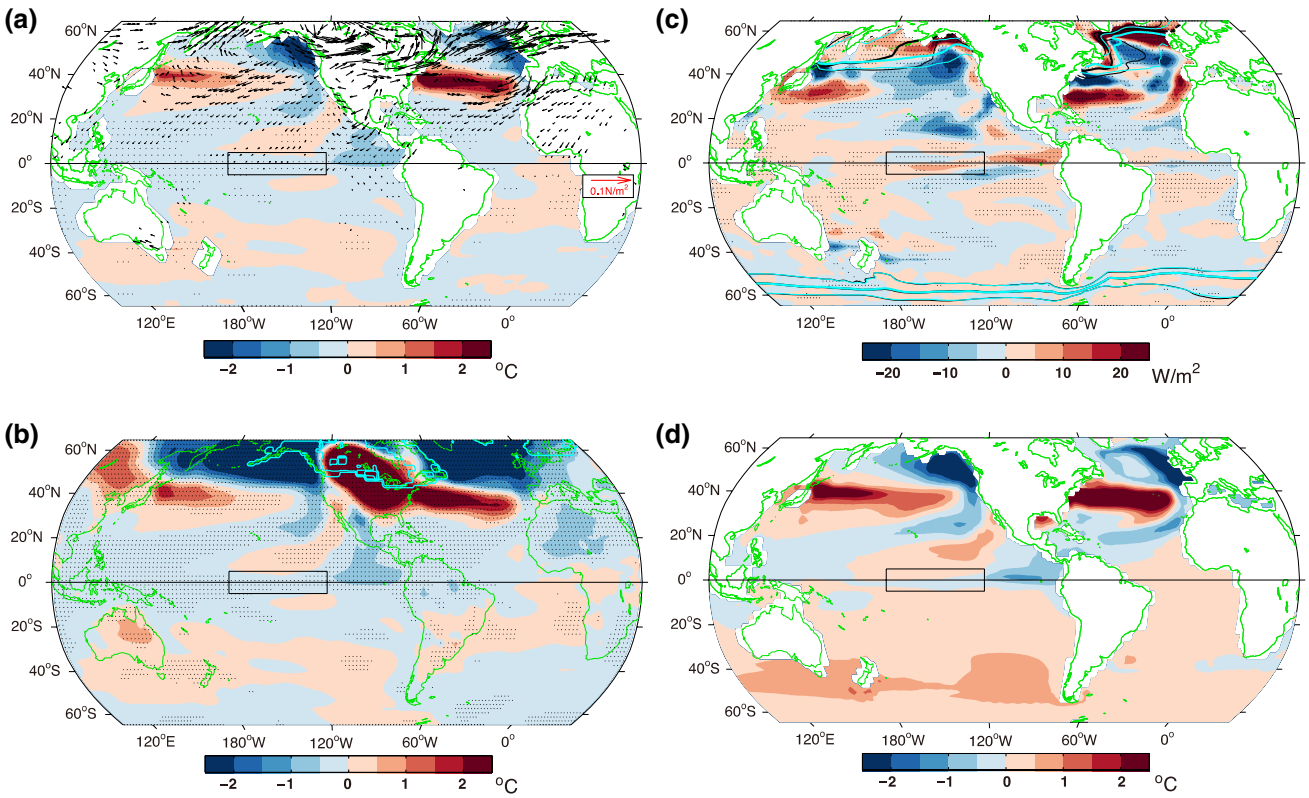

Fig. 11 **a**–**c** Same as Fig. 8 but for the global. **a** SST, wind stress; **b** surface air temperature and ice sheet thickness (*cyan contour* for every 500 m thickness); **c** downward surface heat flux and sea-ice extent. *Black box* shows the location of Nino3.4 region. The *black* and *cyan solid thick lines* in (**c**) represent the annual mean sea-ice extent (>50 % sea ice concentration) before and after 14 ka BP, respectively. *Thin lines* are for September and April sea-ice extent. **d** SST slow response as 13.5–12.5 ka BP decadal mean minus 14.5–15.5 ka BP decadal mean

significantly over the Gulf of Alaska and western North Atlantic (Fig. 11c, thick solid lines for annual mean). The former is supplied from the northern Okhotsk Sea and Bering Sea while the latter is from Baffin Bay and Davis Strait and the Nordic sea, which are sealed by sea ice throughout the year (Fig. 11c, thin solid lines for April/September).

As a result of increased sea-ice extent, the overall spatial pattern of SST, SAT and surface heat flux is changed significantly in the North Atlantic and North Pacific (Fig. 11a–c). The uniform cooling of SST and SAT extends over the NH subpolar marginal sea (Fig. 11a, b, shading) and is amplified by the positive sea-ice albedo feedback. Upward heat flux from ocean to atmosphere is cut off by sea-ice cap that induces net downward anomalies, and a large gradient occurs over the adjacent ice-free ocean surface (Deser et al. 2000) (Fig. 11c, shading). The surface heat flux anomalies dominate the changes of heat absorbed by the atmospheric column (Fig. S2, Supplementary material 2), and the dipole anomaly substantially dampens the heating caused by ice sheet retreat while highlighting the associated cooling effect over the latitudinal band of sea ice expansion to the north of warming. This rapid cooling in the NH may also contribute to the initial trigger in the subtropical north Pacific, which in turn influences the tropics through the WES feedback (Fig. 12). However, we are unable to separately identify the equatorward propagation of the cooling effect induced by jet stream northward shift or sea-ice expansion because all the fast responses are mixed.

5 Discussion

5.1 The role of AMOC

The change of ENSO may also be contributed by a changing AMOC, as proposed by Timmermann et al. (2007b). In ICE, the AMOC is slowed down with the ice-sheet retreat (Fig. 1c; Zhu et al. 2014). Anomalous SST of 13 ka BP departing from 15 ka BP (Fig. 11d) demonstrates a spatial pattern almost identical to the fast response (Fig. 11a) in the NH. The difference emerges as a considerable warming over the SH, hence developing a bi-polar seesaw (Dong and Sutton 2002). This suggests that the slow AMOC decrease (compared with fast wind shift, sea-ice expansion and efficient ocean–atmosphere coupling) through an increased sea-ice concentration in the North Atlantic deep

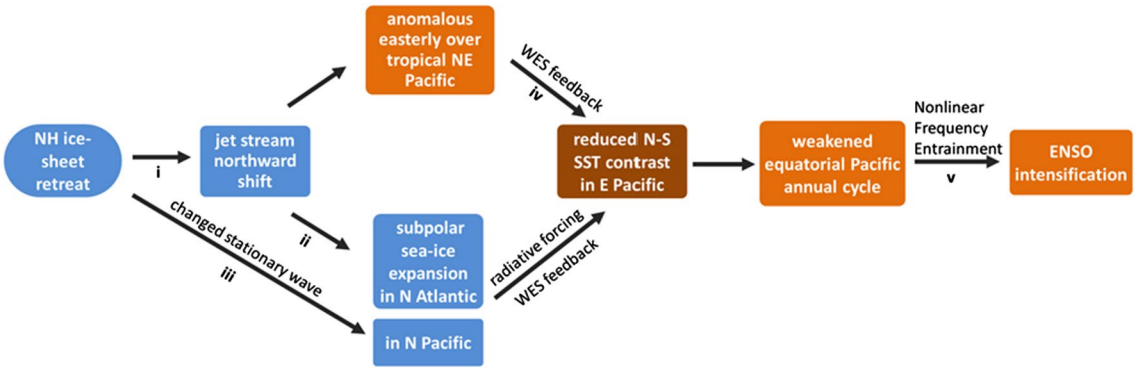

Fig. 12 Schematic of the influence of the lowering of continental ice sheets on ENSO. *Rectangular with blue color* are for responses in mid/high latitude; *orange color* for the tropics. The list below summarizes the references related to the mechanisms. *i* COHMAP 1988; Li and Battisti 2008; Eisenman et al. 2009; Pausata et al. 2011; Lee et al. 2014; Zhang et al. 2014, *ii* Vettoretti and Peltier 2013; Zhang et al. 2014; Zhu et al. 2014, *iii* Bartlein et al. 1998; Otto-Bliesner et al. 2003, *iv* Xie and Philander 1994; Xie 1999, *v* Chang et al. 1994, 1995; Gu and Philander 1995; Liu 2002; Guilyardi 2006; Timmermann et al. 2007a, b; Liu et al. 2014

water formation region can generate a SSTA seesaw pattern in the tropical Atlantic, and in turn, tropical Pacific through the atmospheric teleconnection (Zhang and Delworth 2005; Wu et al. 2005). It reinforces the initial Pacific interhemispheric SST anomaly generated by the fast response.

However, as discussed before in Fig. 7, the AMOC is slowed several decades later and therefore cannot be responsible for the initial fast response. In addition, a closer inspection of the dipole anomaly shows a warming in the equatorial southeastern Pacific, the same magnitude as in the tropical Atlantic, with a ~1.5 °C S–N SST difference in both oceans (Fig. 11d). This is in contrast to the previous studies of SST response to AMOC change, where the tropical Pacific SST anomaly is only about half of that in the tropical Atlantic (cf. Zhang and Delworth 2005; Timmermann et al. 2007b). Therefore, the weakening AMOC may help to reinforce the tropical Pacific SST response on multi-decadal time scales, but is unlikely the leading cause of the abrupt weakening of annual cycle and in turn the abrupt intensification of ENSO at 14 ka BP.

5.2 The abruptness at 14 ka BP

Our model results show that the influence of ice-sheet retreat on the global synchronous climate change is region/topography dependent, and only after exceeding a threshold can abrupt changes occur. Although the ice sheet continues to decrease in both its spatial extent and thickness over the North American continent in the ICE simulation, we only observe the one-step shift of jet stream at 14 ka BP (Fig. 10a) when the LIS decays the greatest (Fig. 1a). The sea-ice extent in the NH subpolar region also significantly increases only at 14 ka BP (Figs. 1c, 7c), implying that the reorganized atmospheric stationary wave associated with the altered wind field and sea-ice transport highly relies on topography and land-sea distribution.

A validation of this argument is the muted global response to ice-sheet lowering in Antarctica. Unlike North America, the spatial features of Antarctica ice sheets which are restricted within relatively higher latitude (say, higher than 70°S) make the intensive receding of ice sheet in the SH at 12 ka BP (Fig. 1a, a half magnitude of ice volume loss as the LIS at 14 ka BP) and interfere little with general atmospheric circulation in the mid/low-latitudes (figure not shown). The consequent mid/low-latitude wind field anomalies, AMOC strength, sea-ice extent in the southern ocean and ENSO amplitude are almost inconspicuous at 12 ka BP. Similarly, global climate and ENSO undergo muted responses during other periods even when ice-sheet volume loss in the NH has the same magnitude as 14 ka BP (Fig. 1a), like 17–14 and 13–6 ka BP. One hypothesis is that the ice-sheet change at 14 ka BP is special for producing a threshold behavior because of the ice-sheet location, over which the abruptly reduced ice thickness somehow favors the buildup of transition of mean climate and, eventually, the tropical interannual climate variability. During 17–14 ka BP, the Fennoscandian ice sheet receding accounts for most of the ice-sheet reduction; through the 13–6 ka BP deglaciation, the ice-sheet receding occurs in a somewhat more northeastward region (relative to that at 14 ka BP) of LIS and at a much slower rate. Neither seems to be able to cause a significant change in global climate. Future studies with sensitive experiments (e.g., to abruptly change ice sheets of 13–6 ka BP as 14 ka BP and to force the coupled model to compare with the current results), are needed to verify this hypothesis.

5.3 Responses of model-dependence

It should be pointed out that our result could be model-dependent. Indeed, our study seems to be inconsistent with

the implications of some previous work (e.g., Chiang and Bitz 2005; Broccoli et al. 2006; Lee et al. 2014). They suggest that a retreat of NH ice sheet should lead to a warming in the NH and in turn north of the equator in the tropical Pacific (and Atlantic), which would prefer an increased equatorial asymmetry and a stronger annual cycle. A more systematic study is needed to identify the cause of the difference. Here, we speculate the cooling in the North Pacific is due to two indirect effects caused by the ice-sheet lowering in our ocean model: the sea ice feedback and the AMOC change. In our model, although the retreating ice sheet induces robust local warming, the changed wind stress and a consequent strong sea-ice expansion in the North Pacific and Atlantic (as discussed before in Figs. 1c, 7c, 11c, Supplementary material 2) generates a robust cooling that may have overwhelmed the direct warming effect. The ice-sheet retreat also slows down the AMOC, which helps to reinforce a bipolar seesaw response with a cooling north of the equator. The anomalous indirect cooling, especially in North Pacific, is somehow replicated in other ice-sheet forcing simulations (e.g., Timm and Timmermann 2007; Smith and Gregory 2012; Lee et al. 2014). These two indirect effects may yet have not fully developed in these simulations due to less model physical complexity and/or prescribed sea ice, therefore bringing contradiction to the responses in the tropical Pacific (e.g., the N–S SST gradient change in the eastern Pacific).

We have observed a nonlinear response of NH jet stream with an abrupt northward displacement at 14 ka BP when the LIS is lowered below an intermediate height (~58 % of its 19 ka BP thickness in ICE-5G), and this displacement is likely the trigger for the abrupt change of coupled ocean–atmosphere system in the tropical eastern Pacific. In fact, the first-order change of NH westerly jet is almost characteristic in simulations forced by the ice-sheet retreat. The direction of shift in our model coincides with COHMAP (1988) (their 18 ka-present), Li and Battisti (2008) (for most of PMIP1 models, PD-LGM), Eisenman et al. (2009) (their LARGE–MEDIUM) and Lee et al. (2014) (their Ice100/75/50-Ice0), except for Pausata et al. (2011) (their PI vs. LGM) and Zhang et al. (2014) (only for zonal wind stress response). Among them, threshold behaviors in Hadley cell change (Lee et al. 2014) and AMOC/sea ice change (Zhang et al. 2014) are found in the two transient runs, implying the nonlinearity in global climate to ice-sheet forcing at the intermediate height, but they are unlike the nonlinear shift of jet stream in our simulation.

6 Conclusion

The climate model with interactive sea ice and ocean dynamics helps to give us a broader picture on how the tropical interannual climate variability and mean climate react to the extratropical ice-sheet topographical and thermal forcings that modifies the asymmetry of the global climate system both directly and indirectly. A schematic summary on the process and a list of related references are depicted in Fig. 12. We find an abrupt increase of ENSO strength in response to the lowering of LIS at 14 ka BP, in the transient simulation forced by the ice-sheet retreat of the last deglaciation. The ENSO intensification is not caused by the increased ocean–atmosphere feedback. Instead, it is caused by its interaction with the weakened annual cycle through the nonlinear mechanism of frequency entrainment. The annual cycle is suppressed by the reduced cross-equatorial SST contrast in the eastern Pacific under the extratropical forcing. The fact is that the equatorial northeast Pacific cools despite the decaying LIS that induces substantial local and downwind warming in the NH. Previous studies in regard of the interhemispheric heat asymmetry suggest removing NH ice sheet should result in a mean ITCZ shifting towards warmer north away from the equator (on the first order). The simulation in our study provides evidence that it might not work because the competing cooling effect of sea-ice compensation (~of the same magnitude as ice sheet) just north of the ice sheet which could be amplified by the sea-ice albedo feedback. In that sense, the jet stream shift associated with the topographic forcing becomes important to the contribution of thermal gradient as a direct effect. Further details are revealed that within a few years as the LIS is lowered across a threshold, the NH westerly jet shifts northward, which then generates a surface easterly wind anomaly in the tropics that increases the trade wind through the WES feedback and therefore cools the tropical northeastern Pacific. As for the indirect effect of rapid sea ice expansion over the NH subpolar region especially North Pacific sector, it is actually induced by the topographic forcing of lowering of LIS that alters the wind stress and thus the sea-ice transport. At last, although AMOC reduce can potentially paly a role in generating a interhemispheric asymmetry of thermal forcing by warming the south and cooling the north, it is difficult to be linked to the 14 ka BP climate shift as that is done within decades.

Clearly, the impact of ice sheet on global climate still requires further studies, as our results—although self-consistent—could be model-dependent. It is well known that models differ in their simulation of ENSO, and the results shown here are based on CCSM3. In particular, models disagree noticeably about changes in ENSO strength in the LGM simulation. For example, the uncertainty of the modeled ENSO amplitude in the LGM is twice as large as in mid-Holocene (Masson-Delmotte et al. 2013) and we do not know how much of the difference comes from ice-sheet forcing. The sensitivity of separated climate system

components to the changed ice sheets and their direct or indirect influences on the tropical climate variability need to be investigated through more sophisticated and systematic numerical experiments.

Acknowledgments The authors thank two anonymous reviewers for helpful comments on the earlier version of this paper. This work is supported by Chinese NSFC41130105 and MOST2012CB955200 and US NSF and DOE. We also gratefully acknowledge financial support from the China Scholarship Council.

References

Bartlein PJ et al (1998) Paleoclimate simulations for North America over the past 21,000 years features of the simulated climate and comparisons with paleoenvironmental data. Quat Sci Rev 17:549–585

Broccoli AJ, Dahl KA, Stouffer RJ (2006) Response of the ITCZ to Northern Hemisphere cooling. Geophys Res Lett. doi:10.1029/2005GL024546

Budikova D (2009) Role of Arctic sea ice in global atmospheric circulation: a review. Glob Planet Change 68:149–163

Carré M et al (2014) Holocene history of ENSO variance and asymmetry in the eastern tropical Pacific. Science 345:1045–1048

Chang B, Wang T Li, Ji L (1994) Interactions between the seasonal cycle and the Southern Oscillation—frequency entrainment and chaos in a coupled ocean–atmosphere model. Geophys Res Lett 21:2817–2820

Chang L, Ji B Wang, Li T (1995) Interactions between the seasonal cycle and El Nino–Southern Oscillation in an intermediate coupled ocean–atmosphere model. J Atmos Sci 52:2353–2372

Chiang JC, Bitz CM (2005) Influence of high latitude ice cover on the marine Intertropical Convergence Zone. Clim Dyn 25:477–496

Clark PU, Alley RB, Pollard D (1999) Northern Hemisphere ice-sheet influences on global climate change. Science 286:1104–1111

Clement AC, Seager R, Cane MA (2000) Suppression of El Niño during the Mid-Holocene by changes in the Earth's orbit. Paleoceanography 15:731–737

Cobb KM et al (2013) Highly variable El Niño–Southern Oscillation throughout the Holocene. Science 339:67–70

COHMAP, COHMAP project members (1988) Climatic changes of the last 18,000 years: observations and model simulations. Science 241:1043–1052

Collins M et al (2010) The impact of global warming on the tropical Pacific Ocean and El Niño. Nat Geosci 3:391–397

Conroy JL, Overpeck JT, Cole JE, Shanahan TM, Steinitz-Kannan M (2008) Holocene changes in eastern tropical Pacific climate inferred from a Galápagos lake sediment record. Quat Sci Rev 27:1166–1180

Crowley TJ (1992) North Atlantic deep water cools the Southern Hemisphere. Paleoceanography 7:489–497

Deser C, Walsh JE, Timlin MS (2000) Arctic sea ice variability in the context of recent atmospheric circulation trends. J Clim 13:617–633

Dong BW, Sutton R (2002) Adjustment of the coupled ocean–atmosphere system to a sudden change in the thermohaline circulation. Geophys Res Lett 29:18-11–18-14

Dyke AS (2004) An outline of North American deglaciation with emphasis on central and northern Canada. Dev Quat Sci 2:373–424

Eagle RA et al (2013) High regional climate sensitivity over continental China constrained by glacial-recent changes in temperature and the hydrological cycle. Proc Natl Acad Sci 110:8813–8818

Eisenman I, Bitz CM, Tziperman E (2009) Rain driven by receding ice sheets as a cause of past climate change. Paleoceanography. doi:10.1029/2009PA001778

Gu D, Philander S (1995) Secular changes of annual and interannual variability in the tropics during the past century. J Clim 8:864–876

Guilyardi E (2006) El Niño–mean state–seasonal cycle interactions in a multi-model ensemble. Clim Dyn 26:329–348

He F, Shakun JD, Clark PU, Carlson AE, Liu Z, Otto-Bliesner BL, Kutzbach JE (2013) Northern Hemisphere forcing of Southern Hemisphere climate during the last deglaciation. Nature 494:81–85

Jackson C (2000) Sensitivity of stationary wave amplitude to regional changes in Laurentide ice sheet topography in single-layer models of the atmosphere. J Geophys Res 105:24443–24454

Jin FF, Kim ST, Bejarano L (2006) A coupled-stability index for ENSO. Geophys Res Lett. doi:10.1029/2006GL027221

Kim ST, Jin F-F (2011a) An ENSO stability analysis. Part I: results from a hybrid coupled model. Clim Dyn 36:1593–1607

Kim ST, Jin F-F (2011b) An ENSO stability analysis. Part II: results from the twentieth and twenty-first century simulations of the CMIP3 models. Clim Dyn 36:1609–1627

Koutavas A, Joanides S (2012) El Niño–Southern Oscillation extrema in the Holocene and Last Glacial Maximum. Paleoceanography. doi:10.1029/2012PA002378

Lee SY, Chiang JC, Chang P (2014) Tropical Pacific response to continental ice sheet topography. Clim Dyn 44:2429–2446

Li C, Battisti DS (2008) Reduced Atlantic storminess during Last Glacial Maximum: evidence from a coupled climate model. J Clim 21:3561–3579

Liu Z (2002) A simple model study of ENSO suppression by external periodic forcing. J Clim 15:1088–1098

Liu Z, Alexander M (2007) Atmospheric bridge, oceanic tunnel, and global climatic teleconnections. Rev Geophys. doi:10.1029/2005RG000172

Liu Z, Kutzbach J, Wu L (2000) Modeling climate shift of El Nino variability in the Holocene. Geophys Res Lett 27:2265–2268

Liu Z et al (2009) Transient simulation of last deglaciation with a new mechanism for Bølling–Allerød warming. Science 325:310–314

Liu Z, Lu Z, Wen X, Timmermann A, Cobb KM (2014) Evolution and forcing mechanisms of El Niño over the last 21,000 years. Nature 515(7528):550–553

Masson-Delmotte V et al (2013) Ch. 5. In: Stocker TF et al. (eds) Climate Change 2013: The Physical Science Basis. Contribution of Working Group I to the Fifth Assessment Report of the Intergovernmental Panel on Climate Change. Cambridge University Press, Cambridge, pp 383–464

McPhaden MJ, Zebiak SE, Glantz MH (2006) ENSO as an integrating concept in Earth science. Science 314:1740–1745

Meehl GA, Teng H, Branstator G (2006) Future changes of El Niño in two global coupled climate models. Clim Dyn 26:549–566

Meehl GA et al (2007) Global climate projections. In: Solomon S et al (eds) Climate Change, 2007, Ch.10: The Physical Science Basis. Contribution of Working Group I to the Fourth Assessment Report of the Intergovernmental Panel on Climate Change. Cambridge University Press, Cambridge

Moy CM, Seltzer GO, Rodbell DT, Anderson DM (2002) Variability of El Niño/Southern Oscillation activity at millennial timescales during the Holocene epoch. Nature 420:162–165

Neelin JD, Battisti DS, Hirst AC, Jin FF, Wakata Y, Yamagata T, Zebiak SE (1998) ENSO theory. J Geophys Res Oceans (1978–2012) 103:14261–14290

Neelin JD, Jin FF, Syu HH (2000) Variations in ENSO phase locking. J Clim 13(14):2570–2590

Otto-Bliesner BL, Brady EC, Shin SI, Liu Z, Shields C (2003) Modeling El Niño and its tropical teleconnections during the last

glacial-interglacial cycle. Geophys Res Lett. doi:10.1029/2003GL018553

Otto-Bliesner BL, Brady EC, Clauzet G, Tomas R, Levis S, Kothavala Z (2006) Last glacial maximum and Holocene climate in CCSM3. J Clim 19(11):2526–2544

Pausata F, Li C, Wettstein J, Kageyama M, Nisancioglu K (2011) The key role of topography in altering North Atlantic atmospheric circulation during the last glacial period. Clim Past 7:1089–1101

Peltier W (2004) Global glacial isostasy and the surface of the ice-age Earth: the ICE-5G (VM2) model and GRACE. Annu Rev Earth Planet Sci 32:111–149

Philander S, Gu D, Lambert G, Li T, Halpern D, Lau N, Pacanowski R (1996) Why the ITCZ is mostly north of the equator. J Clim 9:2958–2972

Pritchard MS, Bush AB, Marshall SJ (2008) Interannual atmospheric variability affects continental ice sheet simulations on millennial time scales. J Clim 21:5976–5992

Rein B, Lückge A, Reinhardt L, Sirocko F, Wolf A, Dullo WC (2005) El Niño variability off Peru during the last 20,000 years. Paleoceanography. doi:10.1029/2004PA001099

Roe GH, Lindzen RS (2001) The mutual interaction between continental-scale ice sheets and atmospheric stationary waves. J Clim 14:1450–1465

Russell JM et al (2014) Glacial forcing of central Indonesian hydroclimate since 60,000 year BP. Proc Natl Acad Sci 111:5100–5105

Shakun JD et al (2012) Global warming preceded by increasing carbon dioxide concentrations during the last deglaciation. Nature 484:49–54

Smith RS, Gregory J (2012) The last glacial cycle: transient simulations with an AOGCM. Clim Dyn 38:1545–1559

Stocker TF, Johnsen SJ (2003) A minimum thermodynamic model for the bipolar seesaw. Paleoceanography. doi:10.1029/2003PA000920

Timm O, Timmermann A (2007) Simulation of the last 21,000 years using accelerated transient boundary conditions. J Clim 20:4377–4401

Timmermann A, Lorenz S, An S, Clement A, Xie S (2007a) The effect of orbital forcing on the mean climate and variability of the tropical Pacific. J Clim 20:4147–4159

Timmermann A et al (2007b) The influence of a weakening of the Atlantic meridional overturning circulation on ENSO. J Clim 20:4899–4919

Trenberth KE, Branstator GW, Karoly D, Kumar A, Lau NC, Ropelewski C (1998) Progress during TOGA in understanding and modeling global teleconnections associated with tropical sea surface temperatures. J Geophys Res Oceans (1978–2012) 103:14291–14324

Tudhope AW, Chilcott CP, McCulloch MT, Cook ER, Chappell J, Ellam RM, Shimmield GB (2001) Variability in the El Niño–Southern Oscillation through a glacial-interglacial cycle. Science 291(5508):1511–1517

van Oldenborgh GJ, Philip S, Collins M (2005) El Niño in a changing climate: a multi-model study. Ocean Sci Discuss 2:267–298

Vettoretti G, Peltier WR (2013) Last glacial maximum ice sheet impacts on North Atlantic climate variability: the importance of the sea ice lid. Geophys Res Lett 40(24): 6378–6383

Wu L, He F, Liu Z (2005) Coupled ocean–atmosphere response to north tropical Atlantic SST: tropical Atlantic dipole and ENSO. Geophys Res Lett 32:L21712

Xie S-P (1999) A dynamic ocean–atmosphere model of the tropical Atlantic decadal variability. J Clim 12:64–70

Xie S-P, Philander SGH (1994) A coupled ocean–atmosphere model of relevance to the ITCZ in the eastern Pacific. Tellus A 46:340–350

Yeager SG, Shields CA, Large WG, Hack JJ (2006) The low-resolution CCSM3. J Clim 19(11):2545–2566

Zhang R, Delworth TL (2005) Simulated tropical response to a substantial weakening of the Atlantic thermohaline circulation. J Clim 18:1853–1860

Zhang X, Lohmann G, Knorr G, Purcell C (2014) Abrupt glacial climate shifts controlled by ice sheet changes. Nature 512:290–294

Zheng W, Braconnot P, Guilyardi E, Merkel U, Yu Y (2008) ENSO at 6 ka and 21 ka from ocean–atmosphere coupled model simulations. Clim Dyn 30:745–762

Zhu J, Liu Z, Zhang X, Eisenman I, Liu W (2014) Linear weakening of the AMOC in response to receding glacial ice sheets in CCSM3. Geophys Res Lett 41:6252–6258